Optica

Resonant behavior of a single plasmonic helix: supplementary material

KATJA HÖFLICH[1,2,*], THORSTEN FEICHTNER[4], ENNO HANSJÜRGEN[3], CASPAR HAVERKAMP[1,2], HEIKO KOLLMANN[3], CHRISTOPH LIENAU[3], AND MARTIN SILIES[3]

[1]Helmholtz Zentrum für Materialien und Energie Berlin, Hahn-Meitner-Platz 1, D – 14109 Berlin, Germany

[2]Max Planck Institute for the Science of Light

[3]Ultrafast Nano-Optics, Institute of Physics and Center of Interface Science, Carl von Ossietzky Universität Oldenburg, D-26129 Oldenburg, Germany

[4]Nano-Optics & Biophotonics Group, Department of Experimental Physics 5, Röntgen Research Center for Complex Material Research (RCCM), Physics Institute, University of Würzburg, Am Hubland, D-97074 Würzburg, Germany

[*]Corresponding author: katja.hoeflich@helmholtz-berlin.de

> **This document provides supplementary information to "Resonant behavior of a single plasmonic helix,"**
> https://doi.org/10.1364/OPTICA.6.001098.

SI. QUANTIFICATION OF CHIROPTICAL RESPONSE

The strength of the chiroptical response can be quantified in different ways. Optical rotation and ellipticity are typically defined by the polarization ellipse of the transmitted light obtained upon incidence of linearly polarized light [1]. While optical rotation refers to the rotation of the polarization plane, ellipticity is given by the ratio of the major axes of the resulting polarization ellipse. Since both quantities are Kramers-Kronig related, the opto-chiral interaction can be quantified using either of them. The ellipticity can be determined by the difference of the amplitudes of transmitted circularly polarized light according to:

$$\tan\psi = \left(|\mathbf{E}|_{\mathrm{LCP}} - |\mathbf{E}|_{\mathrm{RCP}}\right) / \left(|\mathbf{E}|_{\mathrm{LCP}} + |\mathbf{E}|_{\mathrm{RCP}}\right). \tag{S1}$$

Often the ellipticity ψ is measured in terms of the square roots of the corresponding transmitted intensities of LCP and RCP incident light. It has to be mentioned that this is valid only if the conversion of LCP into RCP and vice versa is negligible. Especially, for the case of plasmonic helices this is not necessarily true [2]. The ellipticity is related to the circular dichroism, which refers to the difference in the extinction coefficients κ_{LCP} and κ_{RCP} for incident LCP and RCP light. Here, special care has to be taken concerning the terminology. In chemistry often the term absorption coefficient is used for κ. In the same manner absorbance is used in chemical literature when actually the extinction (i.e. the sum of absorption and scattering) is measured. The typical experimental measure is the transmittance under LCP and RCP incidence. The corresponding definition in chemistry is the molar extinction coefficient

$$\epsilon^{\mathrm{chem}} = -\frac{1}{cl}\ln T \tag{S2}$$

which is normalized to the molar concentration of molecules per liter c and the optical path length l. In case of large ensembles of plasmonic objects the use this quantity and the resulting relationship to the ellipticity ($\psi\,[\mathrm{mdeg}] = 3300\,(\epsilon_{\mathrm{LCP}} - \epsilon_{\mathrm{RCP}})$) may be

justified in terms of an effective medium. Still, proper normalization is an issue and may lead to arbitrarily high values of ellipticity when omitted [3]. To obtain a reliable comparison between the opto-chiral activity of both chiral matter as well as single chiral objects the dissymmetry factor g can be used [4]. The dimensionless quantity

$$g = \frac{2\left(\epsilon_{\text{LCP}} - \epsilon_{\text{RCP}}\right)}{\epsilon_{\text{LCP}} + \epsilon_{\text{RCP}}}. \tag{S3}$$

is normalized by the total extinction. Since g does not depend on the specific way of normalization of the extinction, it is easily transferable to either extinction coefficient with $\epsilon \propto -\ln T$.

To compare experimentally obtained dissymmetries to the corresponding theoretical values, special care has to be taken. For single scatterers the extinction cross section C_{ext} is defined by integrating the radial projection of the energy transfer rate over the spherical surface A in the far-field and normalized by the incident irradiance (intensity) I_{inc} [5]:

$$C_{\text{ext}} = C_{\text{abs}} + C_{\text{sca}} = -\frac{1}{I_{\text{inc}}} \int_A \mathbf{S} \cdot \mathbf{e}_r dA + \frac{1}{I_{\text{inc}}} \int_A \mathbf{S}_{\text{sca}} \cdot \mathbf{e}_r dA \tag{S4}$$

The Poynting vectors $\mathbf{S}$ and $\mathbf{S}_{\text{sca}}$ describe the energy transfer rates of the total and scattered electromagnetic fields. According to the optical theorem the extinction cross section depends on the scattering amplitude in forward direction only and, hence, determines the decrease of the detector area $A(D)$ by the object due to scattering and absorption in transmission measurements:

$$T^{\text{exp}} = \frac{I_T}{I_{\text{inc}}} = \frac{A(D) - C_{\text{ext}}}{A(D)} \tag{S5}$$

For small values of C_{ext} compared to the detector area, this coincides with the negative decadic logarithm typically taken in optical measurements:

$$C_{\text{ext}}/A(D) \approx \epsilon^{\text{exp}} = -\ln T^{\text{exp}} \tag{S6}$$

In our measurement setup the (virtual) detector area is given by the circular area of the pin hole in the image plane (since this area fills only part of the physical detector area). With $1.63\,\mu m^2$ the detector area has almost the same order of magnitude as the measured cross-sections. Hence, the logarithm enlarges ϵ^{exp} relative to $C_{\text{ext}}/A(D)$. The influence on the dissymmetry factors is minor in our case. Nevertheless, in terms of quantitative comparison of the experiment with numerically or analytically obtained values, we employ the most appropriate choice for the dissymmetry factor given by:

$$g_{\text{Cext}} = g_{1\text{-T}} = \frac{2\left(C_{\text{ext}}^{\text{LCP}} - C_{\text{ext}}^{\text{RCP}}\right)}{C_{\text{ext}}^{\text{LCP}} + C_{\text{ext}}^{\text{RCP}}} = \frac{2\left(T_{\text{RCP}} - T_{\text{LCP}}\right)}{2 - T_{\text{LCP}} - T_{\text{RCP}}}. \tag{S7}$$

Here again, the normalization is carried out with respect to the total extinction. Furthermore, the detector area cancels out making the quantity independent from a specific measurement scheme. Thereby, $g_{1\text{-T}}$ is suitable not only for single particle measurements but also for measurements on ensembles of chiral objects. Physically, both of the dissymmetry factors g and $g_{1\text{-T}}$ account for the fact that the same absolute difference in extinction can be caused by a strong or weak chiroptical response.

In terms of optimizing the opto-chiral interaction, the definition of EM-chirality is very interesting, since it can be sorted in ascending order and provides an upper limit [6]. An object is maximally EM chiral if and only if it is transparent to light of one handedness and does not change the helicity of the fields upon interaction [6]. This mathematical description nicely resembles our choice for the dissymmetry factor $g_{1\text{-T}}$ which achieves its upper bound ± 2 if $T_{\text{LCP}} = 1$ and $T_{\text{RCP}} = 0$ or vice versa. The chemical definition of g is mathematically analogue (since the contained logarithm is monotone) and leads to a value of 0.9 reflecting the choice of the exponential.

Here, it has to be mentioned that employing the transmission to calculate the dissymmetry factor according to [7, 8]

$$g_{\text{T}} = \frac{2\left(T_{\text{RCP}} - T_{\text{LCP}}\right)}{T_{\text{LCP}} + T_{\text{RCP}}}. \tag{S8}$$

contradicts its physical meaning. A generally strongly absorbing material with a small difference in transmission for LCP and RCP incidence provides larger values of g_{T} than a material with the same asymmetry ($T_{\text{LCP}} - T_{\text{RCP}}$) but weaker polarization independent absorption. As a consequence, the definition g_{T} achieves its maximum value of 2 not only for maximally EM chiral objects but also for objects with a strong achiral absorption background and/or polarization conversion (e.g. $T_{\text{LCP}} = 0.1$ and $T_{\text{RCP}} = 0$).

Table S1 shows a comparison of all three dissymmetry factors calculated from the literature values of transmission. The largest dissymmetry values $g_{1\text{-T}}$ for plasmonic systems could be achieved in the near- and infrared region, where metallic losses are negligible[3, 10]. Dielectric chiral metamaterials showed even larger dissymmetry factors[9] but are typically limited to the infrared region. In the visible range silver helices are the near optimum choice providing dissymmetry factors close to 2 in full field simulations with and without substrate (ITO-coated glass). For the given geometrical parameters a single silver helix of 5 turns (without substrate) achieves a maximum dissymmetry of around 1.85 for LCP light of 550 nm and of 1.91 for RCP light at 1000 nm. Interestingly, carbon helices showed remarkable dissymmetry factors as well which deserve further investigation. However, it has to mentioned that these helices already work close to their optimum performance as can be seen from Table S1. The same holds true for the investigated single turn gold helices. The achieved dissymmetry factor in the near-IR is remarkable but already close to the numerically predicted value[13]. Hence, exploiting the full chiroptical potential of silver helices is of great scientific interest for applications in chiral sensing and all-optical information processing.

λ[nm]	g_{T}	g	$g_{\text{1-T}}$	reference
-	2	0.92	2	maximally EM chiral object ($T_{\text{LCP}} = 0$, $T_{\text{RCP}} = 1$)
-	2	0.01	0.01	object with strong achiral background($T_{\text{LCP}} = 0$, $T_{\text{RCP}} = 0.01$)
4300	-1.27	-0.67	-1.56	[9], ensemble of photonic helices from photoresist, not transferable to VIS
3500	1.66	0.74	1.47	[10], ensemble of left-handed gold helices in low loss IR range
600	0.14	0.10	0.33	[7], ensemble of helices from carbon platinum mixture, electron beam writing
640	0.22	0.05	0.06	[7], ensemble of helices from carbon platinum mixture, ion beam writing
995	-0.41	-0.14	-0.21	[7], ensemble of helices from carbon platinum mixture, ion beam writing
700	0.73	0.23	0.34	[11], ensemble of triple helices, platinum carbon mixture, ion beam writing
530	-0.67	-0.11	-0.13	[12], ensemble of helices from carbon platinum mixture, ion beam writing
840	0.27	0.07	0.09	[12], ensemble of helices from carbon platinum mixture, ion beam writing
495	-0.41	-0.12	-0.18	[12], ensemble of helices from carbon, ion beam writing
750	0.5	0.24	0.46	[12], ensemble of helices from carbon, ion beam writing
550	-	-	0.45	this work, silver-coated single helices from electron beam writing
1000	-	-	0.30	this work, silver-coated single helices from electron beam writing
1450	-0.03	-0.028	-0.43	[13], gold-coated single helix with 1 turn in near IR
520	-0.52	-0.19	-0.30	[12], modeled ensemble of helices from carbon
800	0.45	0.23	0.47	[12], modeled ensemble of ensemble of helices from carbon
850	-	-	0.8	[14], modeled core-shell helix ensemble with a-Si shell (transmission spectra not provided)
695	-1.13	-0.51	-0.96	[8], modeled left-handed gold-coated helix array (normalization issues in experiment)
1000	1.64	0.70	1.32	[8], modeled left-handed gold-coated helix array (normalization issues in experiment)
1450	-0.03	0.028	0.5	[13], modeled single gold helix of 1 turn
550	-	-	1.85	this work, modeled single silver helices
1050	-	-	1.91	this work, modeled single silver helices

Table S1. **Overview of the achieved values for different definitions of the dissymmetry factors** The top rows show theoretically achievable values, followed by experimental investigations of ensembles of helices. The next rows display experimental values of single plasmonic helices, followed by numerically calculated values. The values from external references were calculated from printed transmission spectra.
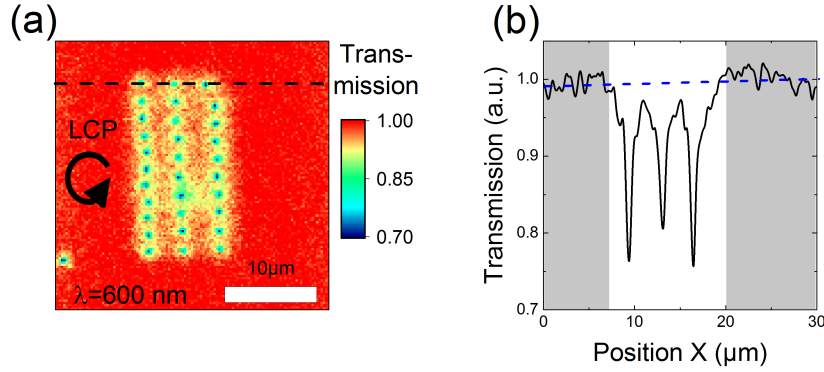
Fig. S1. Normalization scheme of optical transmission measurements (a) Transmission map of an array of 30 helices with 4 pitches at a wavelength of 600 nm for excitation with left-circularly polarized light. The helices are visible by the lowered transmission. (b) Line scan along the black-dashed line in (a) with three helix transmission dips down to 0.75. The spatially-dependent background along the x-axis, indicated by the blue-dashed line is determined by taking into account the grey-shaded regions only.

SII. EVALUATION OF TRANSMISSION MEASUREMENTS

Two-dimensional extinction spectra with a spatial step size of 250 nm and a spectral resolution of 3.7 nm are obtained by raster-scanning the sample with the silver helices through the focus of an all-reflective objective (ARO), resulting in three-dimensional data sets for left and right-circular polarized light. The measurement procedure for each polarization state takes approximately 30 minutes. In Fig. S1 (a), a prototypical transmission map of the array is shown at a wavelength of 775 nm for right-circular polarized light. The spatial resolution of the confocal microscope is improved to approximately 1 μm by placing a 75 μm pinhole in the backfocal plane of the ARO. Afterwards, a position-dependent background signal is subtracted for each of the 137 wavelength intervals that is caused by slight irregularities on the sample substrate, as can be seen in Fig. S1(b) for the line scan shown in (a). The resulting two-dimensional maps for each wavelength are afterwards normalized to the reference transmission spectrum collected using a cover glass as the sample.

In order to quantify the experimental dissymmetry factor g, the total accumulated transmission of each silver helix is essential. However, small spatial fluctuations of the sample during the scanning procedure resulted in slight, but non-negligible variations of the spatial position of the transmission minimum of the silver helices for left- and right-circular polarized light. Hence, the total transmission for each wavelength interval is determined by spatially integrating the transmission in a small region around the transmission minimum and the dissymmetry factor is calculated for every wavelength using equation Eq. (S7). Now, transmission spectra for each silver helix and the respective handedness of incident light are obtained by recomposing the values for each wavelength. Figure S2 shows the transmission spectra (a) and the dissymmetry factor (b) of a prototypical 4 pitch helix. Since here we present single helix measurements the signal to noise ratio is poor. Hence, for the experimental dissymmetries in the main manuscript, all single helix measurements were taken (30 of each geometry) and averaged to avoid any biased selection.
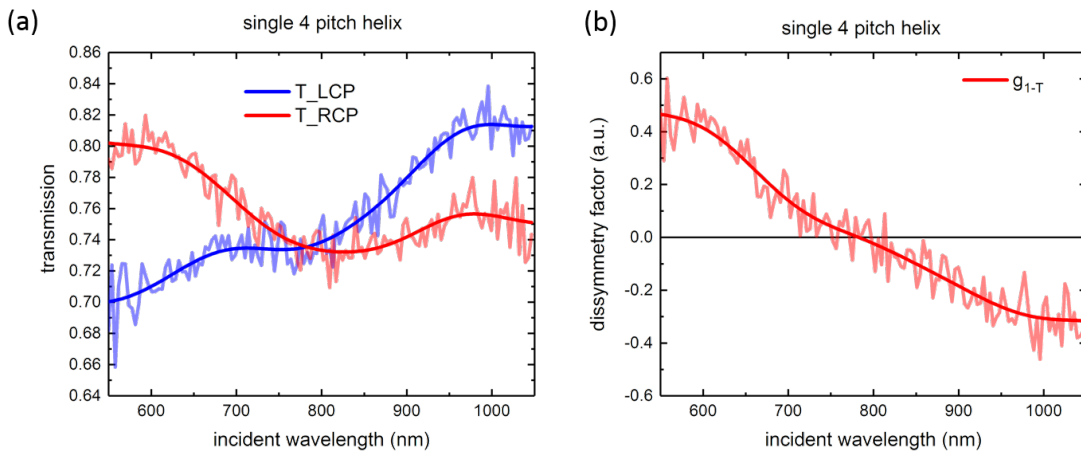
Fig. S2. Single helix measurement a) Transmission measurement of a 4 turn helix and b) resulting dissymmetry factor. The smoothed curves serve as guide for the eye.
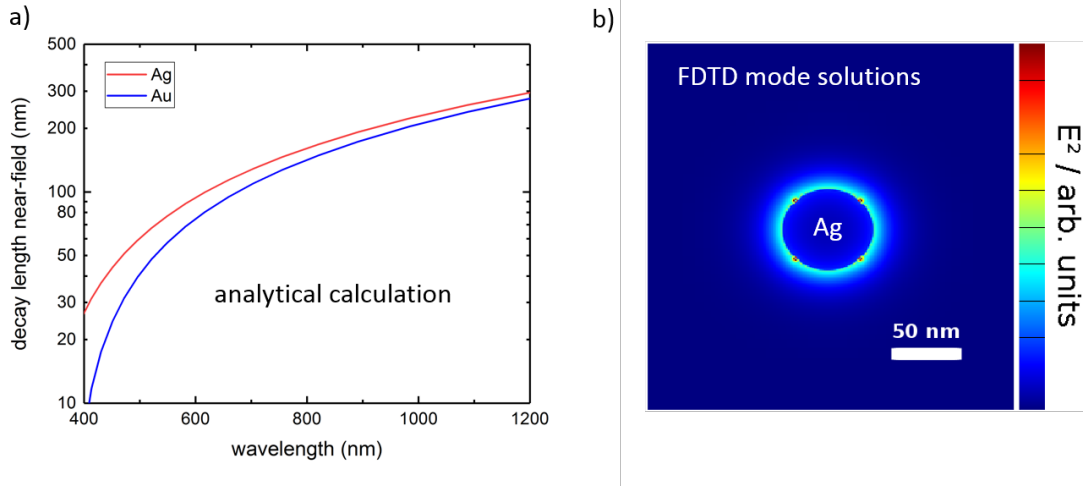
Fig. S3. Decay length of the plasmonic near-field perpendicular to the antenna surface a) The decay length plotted is the distance at which the near-field has decayed by $1/e$. b) Plot of the absolute values of the electric nearfield of the fundamental mode in a infinitely long straight silver wire of radius 32 nm at a wavelength of $\lambda = 400$ nm.

SIII. LINEAR WAVELENGTH SCALING

The calculated eigenmodes of the straight cylindrical wires are justified as helix eigenmodes for negligible interaction of the different helix turns. In other words, if $h >> d_{\text{near-field}}$ defining the distance in which the near-fields decayed by $1/e$. In case of a loss-less Drude model for the permittivity of silver (according to Novotny) with $\epsilon_\infty = 4.0$ and $\omega_p = 9.16$eV this requires a minimum pitch height of 200 nm for the visible range.

Figure S3 shows the wavelengths dependent radial decay of the near field around a cylindrical silver wire of 32 nm radius. The fields are decayed exponentially to $1/e$ at radial distances $\lesssim 200$ nm throughout the visible range. For comparison the vertical decay length for a wire of the same dimensions but from gold is included. To ensure a negligible contribution of the interaction between the different helix turns, the pitch heights of the fabricated helices were chosen to be around 300 nm.

The linear wavelength scaling formalism for short plasmonic wires of Novotny [15] is used within this work. More details can be found in Ref. [16]. Here it is worth mentioning, that both our analytical model and the design tool are neither restricted to a specific material response nor to the linear scaling regime. It is sufficient to know the longitudinal eigenmodes of the cylindrical scatterer, that can be calculated most conveniently for the case of a linear scaling law of the effective wavelength onto the cylinder. The design tool is made available at https://sourceforge.net/projects/plasmonic-helix-1dmodel and implements linear scaling and mode matching. As Fabry-Perot modes with linear scaling law are also present in the single mode regime of a cylindrical dielectric waveguide [17], the considered helix therein may also be dielectric. In that respect, the plasmonic helix serves as an example for our analytical model, promising the strongest chiroptical response in the visible range [6].

SIV. 1D-MODEL

The calculation is performed in the frequency domain, w.l.o.g. assuming time-harmonic fields. By using the phasor formalism, the $e^{-i\omega t}$ terms are suppressed. Poynting's theorem can be used to describe the extinction power P_{ext} when far-field radiation $\mathbf{E}_{\text{inc}}$ excites currents $\mathbf{j}$ in a resonator or an optical antenna [18]:

$$P_{\text{ext},n} = \frac{1}{2}\text{Re}\int_V \mathbf{j}^*(\mathbf{r}) \cdot \mathbf{E}_{\text{inc}}(\mathbf{r})\,\text{d}V\ ,\tag{S9}$$

where * denotes the complex conjugation. The currents can be either the source currents of the electric field $\mathbf{E}_{\text{inc}}$ or, like in our case, the loss currents induced by the external field. For the latter case of extinguished power, equation Eq. (S9) will provide negative values.

To facilitate the calculations, we replace the x-y-plane by the complex plane. For our specific geometry this results in complex quantities in polar form instead of vectors containing trigonometric functions. Two things have to be considered when doing so. First, we write the field and the currents as purely real valued quantities to avoid confusion due to different meanings of the imaginary part. Hence, the complex conjugation in equation Eq. (S9) is obsolete. Still, our observables become complex, now due to our choice of the complex plane. Second, as a consequence the definition of the scalar product in equation Eq. (S9) has to be changed to:

$$P_{\text{ext},n} = \frac{1}{2}\text{Re}\int_V \mathbf{j}(\mathbf{r}) \cdot \mathbf{E}_{\text{inc}}^*(\mathbf{r})\,\text{d}V\ ,\tag{S10}$$

Let us start with the calculation. The transversal excitation field propagates along the z axis and has components pointing in the complex plane only. In our calculation scheme the circularly polarized light $E_x = cos(kz)$ and $E_y = \pm sin(kz)$ read as:

$$E_\varphi(z) = E_0 \cdot e^{\pm ikz}\ .\tag{S11}$$
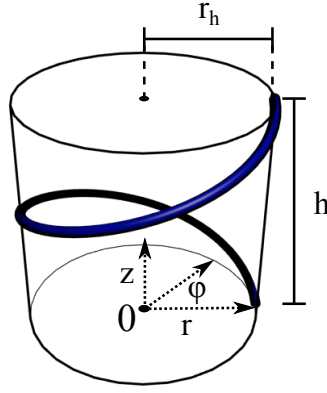
Fig. S4. Geometry of a single pitch of an 1D helix with radius r_h and pitch height h in a cylindrical coordinate system.

with $k = 2\pi/\lambda$ being the k-vector of the free space excitation light with a wavelength of λ and the plus (minus) sign denoting RCP (LCP) light.

The plasmonic helix stretches along the z axis as depicted in Fig. S4. It consists of a one-dimensional wire of length L coiled up to m turns, with r_h being the helix radius and h being the height of a single pitch. The overall height of the helix is $H = m \cdot h$, with a wire length of $L = m\sqrt{4\pi^2 r_h^2 + h^2}$. The lower end of the wire starts at the point $(x, y, z) = (r_h, 0, 0)$. Because of the transversality of the incident field, only the in-plane-component of the helix position vector $\vec{h}$ is needed:

$$h_\varphi = r_h e^{\pm i k_h z} \, , \, z \in [0, H] \, . \tag{S12}$$

Here, we introduced the helix wave vector $k_h = 2\pi/h$ (cf. Fig. 2 c) in the main manuscript). The sign of the exponent again defines the helicity with the plus (minus) sign denoting a right-handed (left-handed) helix.

The direction of the current flow is given by the tangential unit vector at the helix:

$$d_\varphi(z) = \frac{\partial h_\varphi}{\partial z} = \pm i \cdot e^{\pm i k_h z} = e^{\pm i(k_h z + \pi/2)} \, . \tag{S13}$$

Next, we need a description of the scalar current density of the wire modes. The standing waves result from the interference of two counter-propagating waves. Instead of mathematically describing the wave functions onto the helical path, we project them onto the z axis. This is justified since the field components are identical in each point of a respective planar wavefront. The helical geometry is accounted for by vectorial overlap of the tangential helix vector with the fields. Please remember that the product of the tangent with the current density will change sign due to the positive and negative values of the relative charge distributions. Furthermore, it is important to note, that the current density $\mathbf{j}(\mathbf{r})$ turns into a current $j(z)$ upon 1D projection having the physical unit $[j(z)] = 1A$.

Standing waves evolve for multiples of $\lambda/2$ onto the wire length. Here, this is true for the fitting of the projection of the effective wavelength onto the height of the helix: $\lambda_{\text{eff}}^z = 2mh/n$. We therefore define the corresponding wave vector $k_{FP} = n\pi/(mh) = 2\pi/\lambda_{\text{eff}}^z$. Finally, we need to ensure the boundary conditions of vanishing currents at the helix ends $j(H) = j(0) = 0$, leading to:

$$j(z) = j(z)_+ + j(z)_- = \frac{j_0}{2} \cdot \left(e^{i k_{FP} z} - e^{-i k_{FP} z} \right) \tag{S14}$$

The current is a real-valued sine function as required in the discussion above. W.l.o.g. we now choose the helix to be right-handed. The complete description of the current is then:
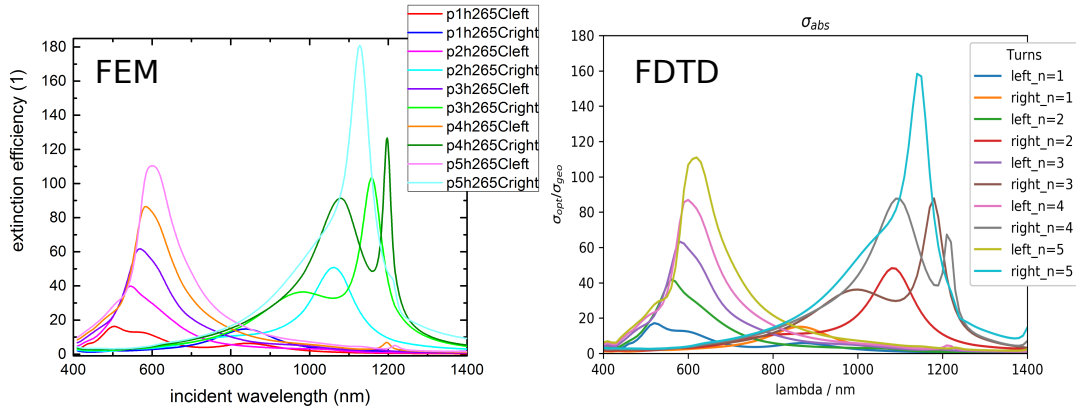
$$j_\varphi(z) = d_\varphi(z) \cdot (j(z)_+ + j(z)_-) = \frac{j_0}{2} \cdot \left(e^{i(k_h z + k_{FP} z)} - e^{i(k_h z - k_{FP} z)} \right) e^{i\pi/2} \tag{S15}$$

The extinction power can then be written as:

$$P_{\text{ext},n} = \frac{1}{2} \text{Re} \int_0^{mh} j_\varphi(z) \cdot E_\varphi^*(z) e^{i\pi/2} \, dz \, , \tag{S16}$$

where the factor $e^{i\pi/2}$ is the phase shift that has to be introduced due to the wire mode being excited at resonance. Finally, we calculate the extinction power according to:

Fig. S5. Comparison between FEM and FDTD numerical results The display the extinction efficiency of silver helices with $1-5$ pitches under left and right circular polarized plane wave illumination.

$$P_{\text{ext}} = \frac{1}{4}\text{Re} \int_0^{mh} j_0 \cdot \left(e^{i(k_h+k_{FP})z} - e^{i(k_h-k_{FP})z} \right) \cdot e^{i\pi/2} \cdot E_0 \cdot e^{\mp ikz} \cdot e^{i\pi/2} \, dz \tag{S17}$$

$$= \frac{1}{4} \int_0^{mh} E_0 \, j_0 \, \text{Re} \left[\left(e^{i(\mp k+k_h+k_{FP})z} - e^{i(\mp k+k_h-k_{FP})z} \right) \cdot (-1) \right] dz \tag{S18}$$

$$= \pm\frac{1}{4} E_0 \, j_0 \int_0^{mh} \cos((k \mp k_h - k_{FP})z) - \cos((k \mp k_h + k_{FP})z) \, dz \tag{S19}$$

$$= \pm\frac{1}{4} E_0 \, j_0 \, mh \left[\text{sinc}((k \mp k_h - k_{FP})mh) - \text{sinc}((k \mp k_h + k_{FP})mh) \right] , \tag{S20}$$

where we used the identity $\cos(-x) = \cos(x)$ and re-sorted the summands. The same result is obtained for real-valued vectorial trigonometric functions when using the sum formulas.

To calculate the numerical values of the overlap integral one needs to know the free space wave length λ, that excites the FP-mode on the helix with a wavelength of λ_{eff}. As required by construction the extinguished power P_{ext} provides negative values for efficient excitation of the induced FP currents. For clarity we plotted the absolute value in Figure 4 of the main manuscript.

SV. NUMERICAL MODELING

Full field electrodynamic modeling was performed using a finite element solver (Comsol Multiphysics) and a finite difference time domain software (Lumerical Solutions). The modeled geometry in both cases was a single helix surrounded by an air domain and perfectly matched layers (PML) both scaled with the incident wavelength. Both techniques showed good agreement of the calculated spectra, cf. Figure S5. Here, the modeled helices had a radius of 75 nm, a pitch height of 265 nm and a wire diameter of 32 nm. Slight differences in the spectra can be attributed to discretization issues in FDTD. The cubic mesh elements coarsen the surfaces and thereby slightly increase scattering losses. Furthermore, the staircase error in FDTD causes a minor red shift of resonances. These issues can be addressed by increasing the mesh resolution at the expense of the computational efforts. The same discretization issues apply for surface charge distributions which we therefore plotted using the FEM software. In FEM the tetragonal meshing provides the best resolution of curved surfaces. Furthermore, the definition of E and B at the same points in space avoids the artificial hotspots which are typically observed on curved surfaces for FDTD (cf. Figure S3 b)). Therefore, all numerical spectra and surface charge plots shown in the main manuscript were calculated using FEM. After validating the models, FDTD was employed for a helix onto an ITO-coated glass substrate. Due to the high aspect ratios of the helices, the substrate showed almost no influence on the observed spectral features. The absorption of ITO and glass in the visible range is negligible and, hence, was the difference in dissymmetry (cf Figure S6 a) for the direct comparison of dissymmetry factors). For performance reasons, all further simulations were carried out without substrate.

In the modeling, large parameter sets were tested including radii of helix and wire, height and number of pitches as well as the helix material, see also Fig. S6. These calculations fully support the theoretical considerations. Furthermore, the pitch numbers were continuously increased between their integer values. Figure S6 b) shows the results for varying the pitch number between 3 and 4 in steps of 0.1. Here, the change in the lengths shifts the underlying Fabry-Perot eigenmodes and thereby visualizes the excitation condition derived in the preceding subsection. Figure S7 a) shows the same data of Figure 4 a) in the main manuscript but over an energy scale. Here, the connection between the value of the transfered energy (dot height) and the peak area of the respective mode becomes more obvious. In Figure S7 b) the height of the pitches is varied to show the robustness of the analytical model. Here the silver helices have a radius of 75 nm. As mentioned in the main manuscript only one free parameter is included in the model, that accounts for the near-surface character of the plasmonic currents in higher mode orders. It is implemented by a correction of the helix radius $r + \delta r$, with δr fixed to 10 nm. This means δr was not modified for the comparison in Figure S7 b).
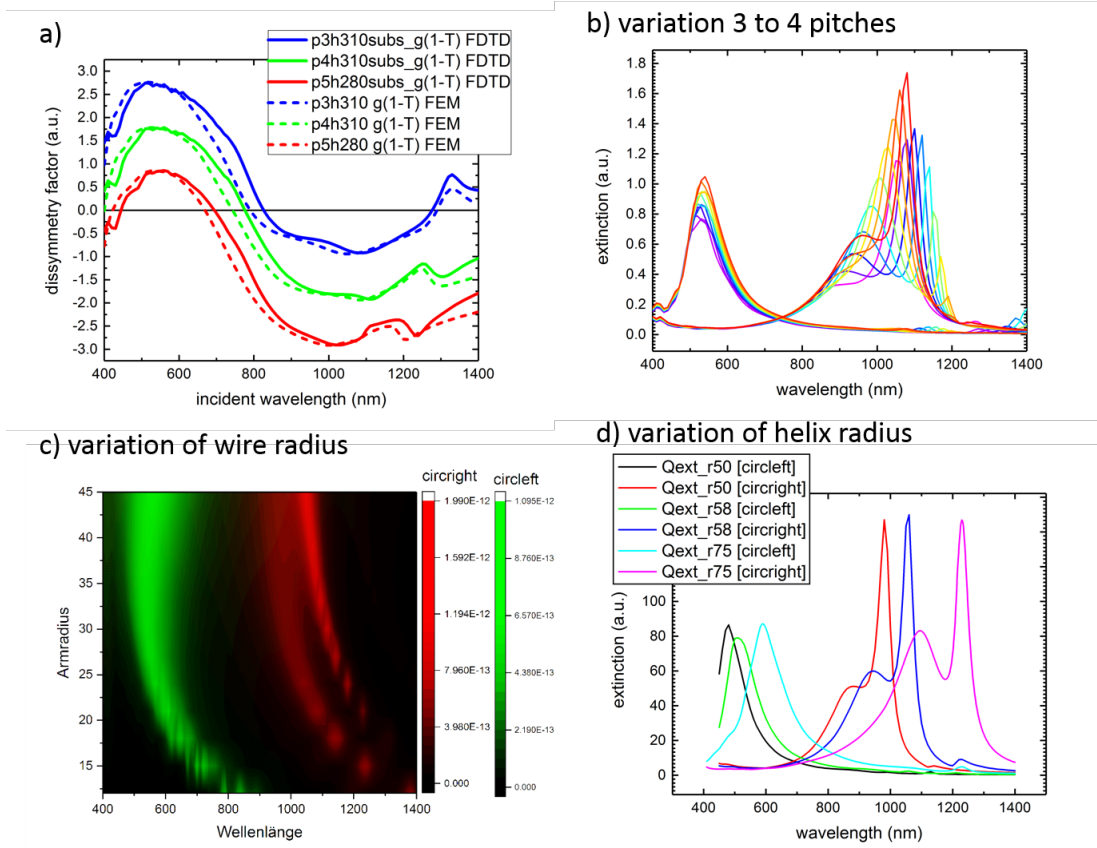
Fig. S6. Further modeling a) comparison of numerically calculated dissymetry factors with and without substrate, b) variation of pitch number visualizing the envelope provided by the helical design tool, c) variation of the wire radius, d) variation of the helix radius.
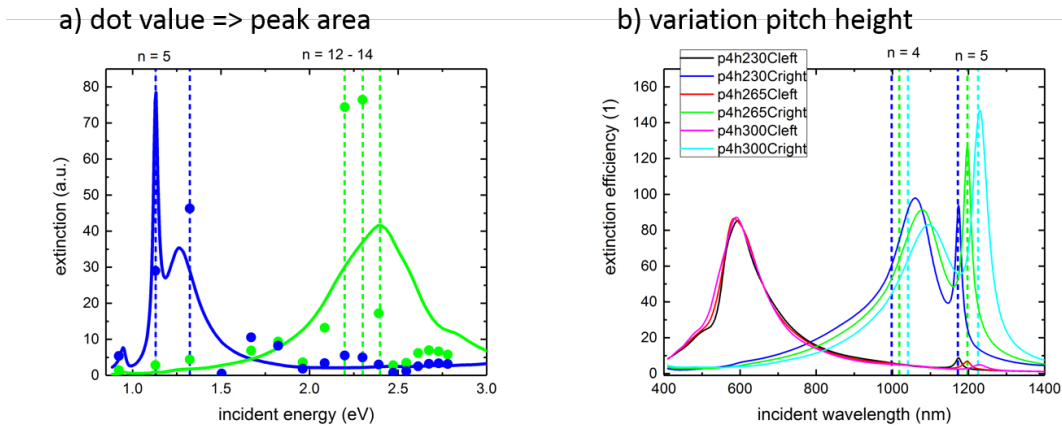
Fig. S7. Comparison to analytical model a) plot of the same data as shown in Figure 4 a) of the main manuscript but over an energy scale, b) variation of the pitch height inlcuding the comparison comparison to the analytical model

REFERENCES

1. L. D. Barron, *Molecular Light Scattering and Optical Activity* (Cambridge University Press, New York, NY, USA, 2009), 2nd ed.
2. J. K. Gansel, M. Wegener, S. Burger, and S. Linden, "Gold helix photonic metamaterials: a numerical parameter study." Opt. Express **18**, 1059–69 (2010).
3. X. Yin, M. Schäferling, B. Metzger, and H. Giessen, "Interpreting chiral nanophotonic spectra: the plasmonic Born-Kuhn model." Nano Lett. **13**, 6238–43 (2013).
4. W. Kuhn, "The physical significance of optical rotatory power," Transactions Faraday Soc. **26**, 293 (1930).
5. C. F. Bohren and D. R. Huffman, *Absorption and Scattering of Light by Small Particles* (John Wiley & Sons, 1983).
6. I. Fernandez-Corbaton, M. Fruhnert, and C. Rockstuhl, "Objects of maximum electromagnetic chirality," Phys. Rev. X **6**, 1–13 (2016).
7. M. Esposito, V. Tasco, and M. Cuscuna, "Nanoscale 3D Chiral Plasmonic Helices with Circular Dichroism at Visible Frequencies," ACS Photonics **17** (2014).
8. D. Kosters, A. de Hoogh, H. Zeijlemaker, H. Acar, N. Rotenberg, and L. Kuipers, "Core-Shell Plasmonic Nanohelices," ACS Photonics p. acsphotonics.7b00496 (2017).
9. M. Thiel, H. Fischer, G. von Freymann, and M. Wegener, "Three-dimensional chiral photonic superlattices." Opt. Lett. **35**, 166–8 (2010).
10. J. K. Gansel, M. Thiel, M. S. Rill, M. Decker, K. Bade, V. Saile, G. von Freymann, S. Linden, M. Wegener, and G. v. Freymann, "Gold helix photonic metamaterial as broadband circular polarizer." Science. **325**, 1513–5 (2009).
11. M. Esposito, V. Tasco, F. Todisco, M. Cuscunà, A. Benedetti, D. Sanvitto, and A. Passaseo, "Triple-helical nanowires by tomographic rotatory growth for chiral photonics," Nat. Commun. **6**, 6484 (2015).
12. M. Esposito, V. Tasco, F. Todisco, M. Cuscun??, A. Benedetti, M. Scuderi, G. Nicotra, and A. Passaseo, "Programmable Extreme Chirality in the Visible by Helix-Shaped Metamaterial Platform," Nano Lett. **16**, 5823–5828 (2016).
13. P. Woźniak, I. De Leon, K. Höflich, C. Haverkamp, S. Christiansen, G. Leuchs, and P. Banzer, "Chiroptical response of a single plasmonic nanohelix," Opt. Express **26**, 1513–1515 (2018).
14. H. J. Singh and A. Ghosh, "Large and tunable chiro-optical response with all dielectric helical nanomaterials," ACS Photonics **5**, acsphotonics.7b01455 (2018).
15. L. Novotny, "Effective Wavelength Scaling for Optical Antennas," Phys. Rev. Lett. **98**, 1–4 (2007).
16. W. Su, X. Li, J. Bornemann, and R. Gordon, "Theory of nanorod antenna resonances including end-reflection phase," Phys. Rev. B - Condens. Matter Mater. Phys. **91**, 1–5 (2015).
17. V. G. Bordo, "Model of Fabry-Pérot-type electromagnetic modes of a cylindrical nanowire," Phys. Rev. B **81**, 035420 (2010).
18. L. Novotny and B. Hecht, *Principles of nano-optics*, vol. 9781107005 (Cambridge University Press, 2012), 2nd ed.